RESEARCH ARTICLE

WILEY

A low-dissipation third-order weighted essentially nonoscillatory scheme with a new reference smoothness indicator

Yahui Wang[1,2] | **Yulong Du**[3] | **Kunlei Zhao**[1,2] | **Li Yuan**[1,2]

[1]ICMSEC and LSEC, Academy of Mathematics and Systems Science, Chinese Academy of Sciences, Beijing, P. R. China

[2]School of Mathematical Sciences, University of Chinese Academy of Sciences, Beijing, P. R. China

[3]School of Mathematics and Systems Science, Beihang University, Beijing, P. R. China

Correspondence
Li Yuan, Academy of Mathematics and Systems Science, No. 55 Zhongguancun East Road, Beijing 100190, P. R. China.
Email: lyuan@lsec.cc.ac.cn

Summary

The classical third-order weighted essentially nonoscillatory (WENO) scheme is notoriously dissipative as it loses the optimal order of accuracy at critical points and its two-point finite difference in the smoothness indicators is unable to differentiate the critical point from the discontinuity. In recent years, modifications to the smoothness indicators and weights of the classical third-order WENO scheme have been reported to reduce numerical dissipation. This article presents a new reference smoothness indicator for constructing a low-dissipation third-order WENO scheme. The new reference smoothness indicator is a nonlinear combination of the local and global stencil smoothness indicators. The resulting WENO-Rp3 scheme with the power parameter $p = 1.5$ achieves third-order accuracy in smooth regions including critical points and has low dissipation, but numerical results show this scheme cannot keep the ENO property near discontinuities. The recommended WENO-R3 scheme ($p = 1$) keeps the ENO property and performs better than several recently developed third-order WENO schemes.

KEYWORDS

Euler equation, hyperbolic conservation law, nonlinear weight, reference smoothness indicator, third-order accuracy, WENO

1 | INTRODUCTION

Solutions of nonlinear hyperbolic conservation laws often have both discontinuities and smooth small-scale structures. It is necessary for numerical schemes to capture discontinuities without producing spurious oscillations and resolve smooth small-scale structures with high resolution. Among many numerical schemes for hyperbolic conservation laws, weighted essentially nonoscillatory (WENO) schemes have become one of the most popular methods.

WENO schemes as first introduced by Liu et al[1] use a convex combination of all candidate stencils of ENO schemes[2-5] to improve the accuracy in smooth regions of solution without losing the nonoscillatory property of ENO schemes near discontinuities. This combination is performed by weighting the contributions of all local fluxes according to the smoothness of solution on candidate stencils such that the weight of a stencil containing a discontinuity is essentially zero. Jiang and Shu[6] developed the classical finite difference WENO schemes (WENO-JS) by designing a local smoothness indicator, which is the sum of normalized L^2 norms of all the derivatives of the lower-order candidate polynomial. Henrick et al[7] developed the WENO-M scheme in which a mapping function is used to produce new weights from the Jiang-Shu

weights so as to satisfy the sufficient conditions of full order convergence. The WENO-M scheme was extended to 17th order.[8] Borges et al[9] proposed the WENO-Z scheme in which a global higher-order smoothness measurement is incorporated into the construction of the weights. The WENO-Z scheme can recover the full order of accuracy and generate sharper results than the WENO-M scheme due to larger weights being assigned to discontinuous stencils while having almost the same computational cost as the classical WENO-JS method. Kumar et al[10] proposed two variants of fifth-order finite difference WENO schemes of adaptive order. Rathan et al[11] analyzed the weights of the fifth-order finite difference WENO-P scheme developed by Kim et al,[12] and they also obtained a new fifth-order WENO scheme[13] which attains the optimal order of accuracy even at the critical points of smooth solutions where the first and second derivatives vanish but not the third derivative. Seventh to eleventh order WENO-Z schemes were developed.[14-16]

On the other hand, third-order WENO schemes received less attention. The reason is that the classical third-order WENO scheme[6] is too dissipative and its order of accuracy is severely degenerated at critical points.[17] However, third-order WENO schemes are attractive for practical applications due to their simplicity and low computational cost. The problem of excessive dissipation and suboptimal order of convergence may be cured by utilizing the WENO-Z type weights.[9] With this methodology, Wu and Zhao[18] developed an improved third-order WENO scheme (WENO-N3) as a part of the complete formulation of a high-resolution hybrid WENO scheme. They devised a fourth-order reference smoothness indicator τ_{4N} by a linear combination of the candidate and global smoothness indicators. But τ_{4N} is unable to achieve the optimal third-order convergence at critical points. To remedy this flaw, Wu et al[19] slightly modified the reference smoothness indicator as τ_{4Np} with a power p to obtain the WENO-Np3 scheme. Based on the work,[19] Gande et al proposed the WENO-F3 scheme[20] with a reference smoothness indicator τ_{4Fp} that contains the linear combination of the first derivative information of the local and global stencils, and introduced the WENO-MN3 scheme[21] with a variable parameter $\epsilon = \mathcal{O}(\Delta x^2)$ in the weights in order to satisfy the sufficient condition for the optimal order convergence. However, Zeng et al[22] remarked that a grid size Δx dependent parameter ϵ makes the numerical solution lose the scale invariance property. Recently, Xu and Wu[23] suggested another fourth-order reference smoothness indicator τ_{4P} such that the resultant WENO-P3 scheme is less dissipative. Nevertheless, the WENO-P3 scheme can only achieve third-order accuracy in smooth regions without critical points. More recently, Xu and Wu[24] used the power $q = 3/4$ on the denominator in the WENO-Z weight formula to recover the optimal convergence order at critical points. Very recently, Bhise et al[25] proposed an efficient hybrid WENO scheme with a problem independent discontinuity locator, and Liu and Shen[26] developed a discontinuity-detecting method for a four-point stencil and applied it to a third-order hybrid WENO scheme.

In this article, we propose a new reference smoothness indicator τ_{4Rp} for improving the third-order WENO scheme where the subscript R represents "root" feature to be explained in Section 3, and p represents the power parameter on the reference smoothness indicator. This reference smoothness indicator is a nonlinear combination of the smoothness indicators of local and global stencils. It has at least fourth-order accuracy in smooth regions and is smaller in magnitude than previous reference indicators τ_{4N}, τ_{4Np}, and τ_{4P}. Theoretical analysis shows that the resultant WENO-Rp3 scheme with the power $p = 1.5$ achieves third-order accuracy in smooth regions including the first-order critical points, but the numerical experiments show that the scheme with $p = 1.5$ produces obvious oscillations around discontinuities, while the scheme with $p = 1$ (named as WENO-R3 scheme) with third-order accuracy in smooth regions without critical points keeps the ENO property and provides more accurate results than several existing third-order WENO schemes: WENO-JS3, WENO-Z3, WENO-N3, and WENO-P3, as well as the third-order MUSCL-LF (Lax-Friedrichs flux) scheme with the Van Leer limiter.[27,28]

The remainder of this article proceeds as follows. Section 2 provides a brief review of the classical third-order WENO schemes for 1D scalar conservation laws. In Section 3, we propose the reference smoothness indicator τ_{4Rp} and analyze the resultant new scheme. Section 4 presents numerical tests to demonstrate the performance of the new scheme, and Section 5 concludes this article.

2 | REVIEW OF THIRD-ORDER WENO SCHEMES

In this section, we briefly describe third-order WENO finite difference schemes for the one-dimensional scalar conservation laws

$$u_t(x, t) + f_x(u(x, t)) = 0. \tag{1}$$

Assume that the grid points $\{x_{j+1/2}\}_{j=0}^N$ are uniformly distributed on a given domain with the grid size $\Delta x = x_{j+1/2} - x_{j-1/2}$. Let $I_j := [x_{j-1/2}, x_{j+1/2}]$ denote a grid cell. The center of I_j is denoted by $x_j = \frac{1}{2}(x_{j-1/2} + x_{j+1/2})$ and the value of a function f at the location x_j is denoted by the subscript j, that is, $f_j = f(x_j)$.

To construct a conservative finite difference for Equation (1), one can define a numerical flux function $h(x)$ implicitly through the following relation,[5]

$$f(x) = \frac{1}{\Delta x} \int_{x-\Delta x/2}^{x+\Delta x/2} h(\xi) d\xi. \tag{2}$$

Differentiating (2) with respect to x leads to

$$f_x(x) = \frac{1}{\Delta x} \left(h\left(x + \frac{\Delta x}{2}\right) - h\left(x - \frac{\Delta x}{2}\right) \right). \tag{3}$$

Thus, Equation (1) can be approximated by a system of ordinary differential equations, where the spatial derivative can be approximated by a conservative finite difference, yielding the semidiscrete form:

$$\frac{du_j}{dt} = -\frac{1}{\Delta x} \left(\hat{f}_{j+\frac{1}{2}} - \hat{f}_{j-\frac{1}{2}} \right), \tag{4}$$

where $u_j(t)$ is the numerical approximation to the point value $u(x_j, t)$, and $\hat{f}_{j\pm 1/2}$ are consistent numerical fluxes which should approximate $h(x_{j\pm 1/2})$ to a high order, for example, $\hat{f}_{j\pm 1/2} = h(x_{j\pm 1/2}) + \mathcal{O}(\Delta x^3)$.

In this article, we apply the local Lax-Friedrichs flux splitting at each grid point,

$$f^{\pm}(u_j) = \frac{1}{2} \left(f(u_j) \pm \alpha u_j \right), \tag{5}$$

where $\alpha = \max_u |f'(u)|$ over the pertinent range of u. The WENO scheme reconstructs high-order numerical fluxes $\hat{f}_{j+1/2}^{\pm}$ from a given point value set $\{f_j^{\pm}\}$. The final numerical flux is given by

$$\hat{f}_{j+\frac{1}{2}} = \hat{f}_{j+\frac{1}{2}}^{+} + \hat{f}_{j+\frac{1}{2}}^{-}. \tag{6}$$

Hereafter, we only describe how $\hat{f}_{j+1/2}^{+}$ is reconstructed because the formulas for $\hat{f}_{j+1/2}^{-}$ are symmetric to $\hat{f}_{j+1/2}^{+}$ with respect to $x_{j+1/2}$. Also, for simplicity, we drop the "+" sign in the superscript.

2.1 | Third-order WENO schemes

To obtain $\hat{f}_{j+1/2}$, the classic third-order WENO scheme uses a global three-point stencil which is subdivided into two two-point substencils as shown in Figure 1. A local numerical flux polynomial approximation $\hat{f}^{(k)}(x)$ satisfying $\hat{f}^{(k)}(x) = h(x) + \mathcal{O}(\Delta x^2)$ with $k \in \{0, 1\}$ is constructed for each of the two substencils by using Equation (2). The second-order candidate numerical fluxes $\hat{f}_{j+1/2}^k$ are given by

$$\begin{aligned}
\hat{f}_{j+\frac{1}{2}}^0 &= -\frac{1}{2}f_{j-1} + \frac{3}{2}f_j, \\
\hat{f}_{j+\frac{1}{2}}^1 &= \frac{1}{2}f_j + \frac{1}{2}f_{j+1},
\end{aligned} \tag{7}$$

which are combined to define the numerical flux of the scheme,

$$\hat{f}_{j+\frac{1}{2}} = \sum_{k=0}^{1} \omega_k \hat{f}_{j+\frac{1}{2}}^k. \tag{8}$$
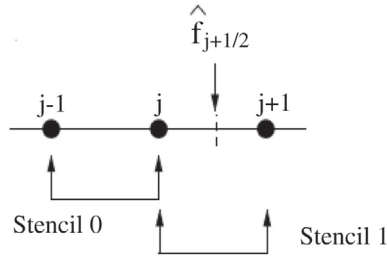
FIGURE 1   Stencils for the third-order WENO numerical flux $\hat{f}_{j+1/2}$

The nonlinear weights ω_k are defined as convention,

$$\omega_k = \frac{\alpha_k}{\sum_{l=0}^{1} \alpha_l} \quad \text{and} \quad \alpha_k = \frac{d_k}{(\beta_k + \epsilon)^2}, \tag{9}$$

where the constant coefficients d_k are called ideal weights since their linear combination with $\hat{f}_{j+1/2}^{k}$ retains the optimal third-order convergence to $h(x_{j+1/2})$, that is,

$$h(x_{j+1/2}) = \sum_{k=0}^{1} d_k \hat{f}_{j+1/2}^{k} + \mathcal{O}(\Delta x^3).$$

The specific values of d_k are as follows (eg, see Reference 29):

$$d_0 = \frac{1}{3}, \quad d_1 = \frac{2}{3}. \tag{10}$$

ϵ in Equation (9) is a small positive parameter introduced to prevent division by zero, and $\epsilon = 10^{-6}$ is used in the classical WENO-JS3 scheme. β_k is the smoothness indicator of the stencil k. The smoothness indicator proposed by Jiang and Shu[6] is given by

$$\beta_k = \sum_{l=1}^{1} \int_{x_{j-1/2}}^{x_{j+1/2}} \Delta x^{2l-1} \left(\frac{d^l}{dx^l} \hat{f}^{(k)}(x) \right)^2 dx. \tag{11}$$

These indicators take on an explicit form:

$$\beta_0 = (f_{j-1} - f_j)^2, \quad \beta_1 = (f_j - f_{j+1})^2. \tag{12}$$

Borges et al[9] proposed the WENO-Z scheme for which the nonlinear weights are

$$\omega_k = \frac{\alpha_k}{\sum_{l=0}^{1} \alpha_l} \quad \text{and} \quad \alpha_k = d_k \left(1 + \left(\frac{\tau_3}{\beta_k + \epsilon} \right)^q \right), \quad k = 0, 1, \tag{13}$$

where $\epsilon = 10^{-40}$, and $\tau_3 = |\beta_1 - \beta_0|$ is a third-order reference smoothness indicator, which drives the weights ω_k in (13) towards the optimal weights d_k faster than the J-S weights (9). The WENO-Z scheme can recover the optimal order at the first-order critical point if the power $q = 2$, but this is more dissipative near discontinuities than $q = 1$, thus in the WENO-Z3 scheme and following modified WENO-Z type schemes, $q = 1$ is used. Then a less dissipative WENO scheme means to use a sufficiently high-order reference smoothness indicator in lieu of τ_3 in Equation (13) .

2.2 | Sufficient condition for third-order convergence

In order to design a suitable reference smoothness indicator for the WENO-Z weights (13), a sufficient condition on weights to recover the optimal order of the third-order WENO scheme is required. The candidate numerical fluxes (7)

can be expanded by Taylor series expansion to get

$$\hat{f}^k_{j+\frac{1}{2}} = h_{j+\frac{1}{2}} + A_k \Delta x^2 + \mathcal{O}(\Delta x^3), \quad k = 0, 1, \tag{14}$$

where the coefficient A_k is independent of Δx. Thus, the WENO flux (8) can be reorganized in the form

$$\begin{aligned} h_{j+\frac{1}{2}} &= \sum_{k=0}^{1} d_k \hat{f}^k_{j+\frac{1}{2}} + \sum_{k=0}^{1} (\omega_k - d_k) \hat{f}^k_{j+\frac{1}{2}} \\ &= \sum_{k=0}^{1} d_k \hat{f}^k_{j+\frac{1}{2}} + \Delta x^2 \sum_{k=0}^{1} A_k (\omega_k - d_k) + \sum_{k=0}^{1} (\omega_k - d_k) \mathcal{O}(\Delta x^3). \end{aligned} \tag{15}$$

A sufficient condition for the scheme to achieve third-order accuracy is

$$\omega_k = d_k + \mathcal{O}(\Delta x^2). \tag{16}$$

Equation (16) is a sufficient condition but not a necessary one. However, this condition provides useful information for the design of high-order reference smoothness indicator. What we attempt to do is, within the weighting framework (13) ($q \equiv 1$), to seek a sufficiently high-order reference smoothness indicator that can satisfy the condition (16).

3 | A NEW REFERENCE SMOOTHNESS INDICATOR

Wu and Zhao[18] introduced a fourth-order reference smoothness indicators τ_{4N} which is a linear combination of the local and global smoothness indicators inspired by the work of Hu et al.[30] Later, Wu et al[19] modified τ_{4N} to τ_{4Np} with a power p in order to recover the optimal order at critical points. Recently, Xu and Wu[23] developed another fourth-order reference smoothness indicator τ_{4P} which contains some quantity from the first derivative of the global smoothness indicator. In this section, we propose a new fourth-order smoothness indicator τ_{4p} which can recover the optimal order at critical points and has lower dissipation. In the above subscripts, "4" means fourth-order accuracy, capital letters "N, P, R" mean "new", "polynomial", and "root" features, respectively, and small letter "p" means "power".

Taylor series expansion of the local smoothness indicators (12) at x_j gives

$$\begin{aligned} \beta_0 &= f_j'^2 \Delta x^2 - f_j' f_j'' \Delta x^3 + \left(\frac{1}{4} f_j''^2 + \frac{1}{3} f_j' f_j''' \right) \Delta x^4 - \left(\frac{1}{12} f_j' f_j^{(4)} + \frac{1}{6} f_j'' f_j''' \right) \Delta x^5 + \mathcal{O}(\Delta x^6), \\ \beta_1 &= f_j'^2 \Delta x^2 + f_j' f_j'' \Delta x^3 + \left(\frac{1}{4} f_j''^2 + \frac{1}{3} f_j' f_j''' \right) \Delta x^4 + \left(\frac{1}{12} f_j' f_j^{(4)} + \frac{1}{6} f_j'' f_j''' \right) \Delta x^5 + \mathcal{O}(\Delta x^6). \end{aligned} \tag{17}$$

Wu and Zhao[18] introduced a "new" (N) reference smoothness indicator of the form

$$\tau_{4N} = \left| \frac{1}{2} (\beta_0 + \beta_1) - \beta_3 \right|, \tag{18}$$

where β_3 is the Jiang-Shu smoothness indicator of the global three-point stencil and is expressed as

$$\beta_3 = \sum_{l=1}^{2} \int_{x_{j-1/2}}^{x_{j+1/2}} \Delta x^{2l-1} \left(\frac{d^l}{dx^l} \hat{f}^{(3)}(x) \right)^2 dx = \frac{13}{12} (f_{j-1} - 2f_j + f_{j+1})^2 + \frac{1}{4} (f_{j-1} - f_{j+1})^2. \tag{19}$$

Taylor series expansion of Equation (19) at x_j gives

$$\beta_3 = f_j'^2 \Delta x^2 + \left(\frac{13}{12} f_j''^2 + \frac{1}{3} f_j' f_j''' \right) \Delta x^4 + \mathcal{O}(\Delta x^6). \tag{20}$$

Using Equations (17) and (20), one can see that Equation (18) can be expanded in smooth regions as

$$\tau_{4\text{N}} = \left| \frac{5}{6} f_j''^2 \right| \Delta x^4 + \mathcal{O}(\Delta x^6). \tag{21}$$

Later, Wu et al[19] slightly modified the reference smoothness indicator (18) with a power p as

$$\tau_{4\text{N}p} = \left| \frac{1}{2}(\beta_0 + \beta_1) - \beta_3 \right|^p, \quad p = 1, 1.5. \tag{22}$$

More recently, Xu and Wu[23] developed a reference smoothness indicator containing a term out of β_3:

$$\tau_{4\text{P}} = \left| \frac{1}{2}(\beta_0 + \beta_1) - \frac{1}{4}(f_{j-1} - f_{j+1})^2 \right|. \tag{23}$$

By using Equation (17) and Taylor expansions of the last term, Equation (23) can be expanded as

$$\tau_{4\text{P}} = \left| \frac{1}{4} f_j''^2 \right| \Delta x^4 + \mathcal{O}(\Delta x^6). \tag{24}$$

In this work, we propose a new reference smoothness indicator $\tau_{4\text{R}p}$ that is a nonlinear combination of the local and global smoothness indicators, Equations (12) and (19). The result is

$$\tau_{4\text{R}p} = \left| \frac{1}{4} \left[3 \left(\beta_0 + \beta_1 \right) - 2\beta_3 \right] - \sqrt{\beta_0 \beta_1} \right|^p, \quad p = 1, 1.5. \tag{25}$$

Here, the subscript "R" stands for the "root" feature in the last term and "p" for the power p. The values $p = 1$ and 1.5 will be explained following Remark 1. By using Equations (17) and (20), we can show that Equation (25) can be expanded as

$$\tau_{4\text{R}p} = \left(\left| \frac{1}{12} f_j''^2 \right| \Delta x^4 + \mathcal{O}(\Delta x^6) \right)^p. \tag{26}$$

Comparing Equation (26) with (24) and (21), we see that the coefficient of the leading term is in the sequence of $\tau_{4\text{R}p} < \tau_{4\text{P}} < \tau_{4\text{N}}$.

Remark 1. The WENO-N3 (18), WENO-Np3 (22), WENO-P3 (23), and WENO-Rp3 (25) schemes can achieve third-order accuracy in smooth regions without the first-order critical point ($f_j' = 0$, $f_j'' \neq 0$). However, the WENO-N3 and WENO-P3 schemes lose the optimal order of accuracy at the critical point while the WENO-Np3 and WENO-Rp3 schemes with the parameter $p = 1.5$ can achieve the optimal order at the critical point.

The conclusion on the WENO-Rp3 scheme in Remark 1 can be got as follows. By inserting Equations (26) and (17) into (13) ($q = 1$), we have

$$\alpha_0 = d_0 \left(1 + \frac{\left(\frac{1}{12} f_j''^2 \Delta x^4 + \mathcal{O}(\Delta x^6) \right)^p}{f_j'^2 \Delta x^2 - f_j' f_j'' \Delta x^3 + \left(\frac{1}{4} f_j''^2 + \frac{1}{3} f_j' f_j''' \right) \Delta x^4 + \mathcal{O}(\Delta x^5)} \right),$$

$$\alpha_1 = d_1 \left(1 + \frac{\left(\frac{1}{12} f_j''^2 \Delta x^4 + \mathcal{O}(\Delta x^6) \right)^p}{f_j'^2 \Delta x^2 + f_j' f_j'' \Delta x^3 + \left(\frac{1}{4} f_j''^2 + \frac{1}{3} f_j' f_j''' \right) \Delta x^4 + \mathcal{O}(\Delta x^5)} \right). \tag{27}$$

Two cases depending on values of f_j' and f_j'' are expressed as follows:

$$\begin{cases} \omega_k = d_k \left(1 + \frac{\left(\frac{1}{12} f_j''^2 \Delta x^4 + \mathcal{O}(\Delta x^6) \right)^p}{f_j'^2 \Delta x^2} \right) = d_k \left(1 + \mathcal{O}(\Delta x^{4p-2}) \right), \; f_j' \neq 0, \\[3mm] \omega_k = d_k \left(1 + \frac{\left(\frac{1}{12} f_j''^2 \Delta x^4 + \mathcal{O}(\Delta x^6) \right)^p}{\frac{1}{4} f_j''^2 \Delta x^4 + \mathcal{O}(\Delta x^5)} \right) = d_k \left(1 + \mathcal{O}(\Delta x^{4p-4}) \right), \; f_j' = 0, f_j'' \neq 0. \end{cases} \tag{28}$$

Comparing Equation (28) with the sufficient condition (16), we can find that the parameter p should satisfy $4p - 2 \geq 2$ in smooth regions without critical points or $4p - 4 \geq 2$ at the first-order critical point to achieve the optimal order of accuracy. Therefore, the new WENO-Rp3 scheme with $p = 1$ can achieve third-order accuracy only in smooth regions without the critical point, while with $p = 1.5$ it can achieve third-order accuracy even at the critical point.

Remark 2. The quantity of dissipation is in the order of WENO-R3 < WENO-P3 < WENO-N3 < WENO-Z3. This can be shown by comparing the present WENO-R3 scheme (ie, WENO-Rp3 with $p = 1$) with the WENO-P3 scheme. Suppose S_c and S_d are two substencils of the same global stencil such that the solution is smoother at S_c than at S_d ($\beta_c < \beta_d$). For $p = 1$, the relative importance of weights are

$$
\begin{aligned}
\left(\frac{\omega_d}{\omega_c}\right)_{\tau_{4R}} - \left(\frac{\omega_d}{\omega_c}\right)_{\tau_{4P}} &= \frac{d_d}{d_c}\left(\frac{1 + \frac{\tau_{4R}}{\beta_d}}{1 + \frac{\tau_{4R}}{\beta_c}} - \frac{1 + \frac{\tau_{4P}}{\beta_d}}{1 + \frac{\tau_{4P}}{\beta_c}}\right) \\
&= \frac{d_d}{d_c}\frac{\beta_d - \beta_c}{\beta_c\beta_d}\frac{\tau_{4P} - \tau_{4R}}{\left(1 + \frac{\tau_{4R}}{\beta_c}\right)\left(1 + \frac{\tau_{4P}}{\beta_c}\right)} > 0,
\end{aligned}
\tag{29}
$$

where the inequality results from $\beta_d > \beta_c$ and $\tau_{4P} > \tau_{4R}$ (compare Equation (26) with (24)). Thus

$$
\left(\frac{\omega_d}{\omega_c}\right)_{\tau_{4R}} > \left(\frac{\omega_d}{\omega_c}\right)_{\tau_{4P}}.
\tag{30}
$$

This implies that the WENO-R3 scheme assigns a larger weight to the nonsmooth stencil than the WENO-P3 scheme, so it is expected to be less dissipative than the latter. Similar comparisons can be done for other schemes.

Remark 3. Although the WENO-Rp3 scheme with the power $p = 1.5$ has third-order accuracy at critical points, we will see that it is prone to numerical overshoots near discontinuities. On the other hand, the recommended WENO-R3 scheme with $p = 1$ will maintain the ENO property well and perform better than other recently developed third-order WENO schemes, even though it is not third-order accurate at the critical points.

4 | NUMERICAL TESTS

In this section, we provide some numerical examples to compare the performances of the present WENO-Rp3 ($p = 1.5$) and WENO-R3 ($p = 1$) schemes and the WENO-JS3, WENO-Z3, WENO-N3, WENO-P3 schemes. We also compare them with the popular third-order MUSCL-LF scheme with the van Leer total variation diminishing (TVD) limiter. The presentation of this section starts with solutions of the advection equation, followed by solutions of the Euler equations. The time advancement is done by using the third-order TVD Runge-Kutta method.[5]

4.1 | Scalar test problems

Consider the scalar advection equation with periodic boundary conditions and different initial data to test the propagation of arbitrary initial profiles, containing jump discontinuities and corner points.

Example 1 (One-dimensional Linear equation). Let us consider the following 1D linear advection equation:

$$
u_t + u_x = 0, \quad -1 \leq x \leq 1, \quad t \geq 0,
\tag{31}
$$

with the initial data

$$
u(x, 0) = u_0(x).
$$

We test the numerical convergence order of the proposed scheme on the linear equation (31) with four sets of initial data

TABLE 1 L^1 errors and convergence rates at $t = 2.0$ of different schemes for the linear advection Equation (31) with the initial data (32a)

	WENO-JS3	WENO-Z3	WENO-N3	WENO-P3	WENO-R3	WENO-Rp3
N	L^1 error (order)	L^1 error (order)	L^1 error (order)	L^1 error (order)	L^1 error (order)	L^1 error (order)
10	0.30E−0(—)	0.23E−0(—)	0.21E−0(—)	0.17E−0(—)	0.14E−0(—)	7.01E−2(—)
20	9.08E−2(1.72)	7.58E−2(1.60)	6.85E−2(1.62)	5.08E−2(1.74)	3.21E−2(2.12)	8.79E−3(3.00)
40	3.83E−2(1.25)	2.07E−2(1.87)	1.66E−2(2.04)	1.20E−2(2.08)	7.67E−3(2.07)	1.21E−3(2.86)
80	9.41E−3(2.03)	4.86E−3(2.09)	3.80E−3(2.13)	2.54E−3(2.24)	1.66E−3(2.21)	1.58E−4(2.94)
160	1.91E−3(2.30)	1.09E−3(2.16)	8.15E−4(2.22)	5.58E−4(2.19)	3.61E−4(2.20)	2.01E−5(2.97)
320	2.70E−4(2.82)	2.53E−4(2.10)	2.04E−4(2.00)	1.31E−4(2.09)	8.14E−5(2.15)	2.57E−6(2.97)

TABLE 2 L^1 errors and convergence rates at $t = 2.0$ of different schemes for the linear advection Equation (31) with the initial data (32b)

	WENO-JS3	WENO-Z3	WENO-N3	WENO-P3	WENO-R3	WENO-Rp3
N	L^1 error (order)	L^1 error (order)	L^1 error (order)	L^1 error (order)	L^1 error (order)	L^1 error (order)
10	0.29E−0(—)	0.25E−0(—)	0.23E−0(—)	0.20E−0(—)	0.17E−0(—)	0.13E−0(—)
20	0.11E−0(1.40)	7.87E−2(1.67)	7.13E−2(1.69)	5.51E−2(1.86)	3.78E−2(2.17)	2.44E−2(2.41)
40	4.21E−2(1.39)	2.44E−2(1.69)	1.91E−2(1.90)	1.35E−2(2.03)	8.87E−3(2.09)	3.35E−3(2.86)
80	1.11E−2(1.92)	5.76E−3(2.08)	4.53E−3(2.08)	3.12E−3(2.11)	2.07E−3(2.10)	4.30E−4(2.96)
160	2.36E−3(2.23)	1.30E−3(2.15)	9.75E−4(2.22)	6.59E−4(2.24)	4.37E−4(2.24)	5.53E−5(2.96)
320	3.52E−4(2.74)	3.19E−4(2.03)	2.38E−4(2.03)	1.72E−5(1.94)	1.15E−5(1.93)	7.01E−6(2.98)

$$\text{(a)} \quad u_0(x) = \sin(\pi x), \quad \text{(b)} \quad u_0(x) = \sin\left(\pi x - \frac{\sin(\pi x)}{\pi}\right),$$

$$\text{(c)} \quad u_0(x) = \sin^2(\pi x), \quad \text{(d)} \quad u_0(x) = \sin^3(\pi x). \tag{32}$$

Since we use the third-order TVD Runge-Kutta method in time, the time step is taken as $\Delta t = 0.5\Delta x$ to be compatible with the spatial order.

Table 1 shows the L^1 errors and convergence rates, respectively, at $t = 2$ for the initial data (32a). We see that the errors decrease with the sequence of WENO-JS3, WENO-Z3, WENO-N3, WENO-P3, WENO-R3, and WENO-Rp3. It is noted that the WENO-Rp3 scheme achieves the optimal third order.

Table 2 shows the results $t = 2$ for the initial data (32b) which contains two first-order critical points at which $f' = 0$, $f'' \neq 0, f''' \neq 0$ in the domain. The numerical convergence order of all the schemes except WENO-Rp3 does not achieve the optimal order due to the occurrence of critical points. In comparison, the present WENO-R3 scheme performs better than the previous WENO schemes.

Table 3 shows the results $t = 2$ for the initial data (32c) which contains a first-order critical point. We see that the errors decrease with the sequence of WENO-JS3, WENO-Z3, WENO-P3, WENO-R3, and WENO-Rp3. The WENO-Rp3 scheme achieves the best accuracy compared with the other schemes.

Table 4 shows the results $t = 2$ for the initial data (32d) which contains first-order and second-order critical points ($f' = 0, f'' = 0$ but $f''' \neq 0$). It is noted that the WENO-Rp3 scheme achieves the optimal third order, while other schemes do not achieve the optimal order. The errors from large to small is still in the sequence of WENO-JS3, WENO-Z3, WENO-P3, WENO-R3, and WENO-Rp3.

Example 2 (Two-dimensional Linear equation). Let us consider the following 2D linear advection equation:

$$u_t + u_x + u_y = 0, \quad 0 \leq x, y \leq 1, \quad t \geq 0, \tag{33}$$

We test the numerical convergence order of the proposed scheme on the linear equation (33) with the initial data

TABLE 3 L^1 errors and convergence rates at $t = 2.0$ of different schemes for the linear advection Equation (31) with the initial data (32c)

N	WENO-JS3 L^1 error (order)	WENO-Z3 L^1 error (order)	WENO-N3 L^1 error (order)	WENO-P3 L^1 error (order)	WENO-R3 L^1 error (order)	WENO-Rp3 L^1 error (order)
10	0.33E−0(—)	0.364E−0(—)	0.364E−0(—)	0.363E−0(—)	0.358E−0(—)	0.336E−0(—)
20	2.31E−1(0.51)	2.08E−1(0.81)	1.94E−1(0.91)	1.66E−1(1.13)	1.34E−1(1.42)	8.58E−2(1.97)
40	7.79E−2(1.57)	5.14E−2(1.99)	4.54E−2(2.10)	3.63E−2(2.19)	2.49E−2(2.43)	1.07E−2(3.00)
80	3.36E−2(1.21)	1.85E−2(1.47)	1.42E−2(1.68)	9.39E−3(1.95)	5.95E−3(2.07)	1.32E−3(3.02)
160	8.05E−3(2.06)	4.26E−3(2.12)	3.15E−3(2.17)	2.14E−3(2.13)	1.34E−3(2.15)	1.69E−4(2.97)
320	1.38E−3(2.54)	9.53E−4(2.16)	6.91E−4(2.19)	4.59E−4(2.22)	3.09E−4(2.12)	2.13E−5(2.99)

TABLE 4 L^1 errors and convergence rates at $t = 2.0$ of different schemes for the 2D linear advection Equation (31) with the initial data (32d).

N	WENO-JS3 L^1 error (order)	WENO-Z3 L^1 error (order)	WENO-N3 L^1 error (order)	WENO-P3 L^1 error (order)	WENO-R3 L^1 error (order)	WENO-Rp3 L^1 error (order)
10	0.263E−0(—)	0.243E−0(—)	0.235E−0(—)	0.215E−0(—)	0.193E−0(—)	0.169E−0(—)
20	2.10E−1(0.32)	1.94E−1(0.32)	1.85E−1(0.35)	1.69E−1(0.35)	1.52E−1(0.34)	1.27E−1(0.41)
40	9.20E−2(1.19)	5.81E−2(1.74)	5.03E−2(1.88)	4.16E−2(2.02)	3.43E−2(2.15)	2.49E−2(2.35)
80	2.84E−2(1.70)	1.52E−2(1.93)	1.12E−2(2.17)	8.05E−3(2.37)	5.80E−3(2.56)	3.24E−3(2.94)
160	7.93E−3(1.84)	3.42E−3(2.15)	2.46E−3(2.19)	1.72E−3(2.23)	1.18E−3(2.30)	4.12E−4(2.98)
320	1.42E−3(2.48)	7.46E−4(2.20)	5.32E−4(2.21)	3.60E−4(2.26)	2.58E−4(2.19)	5.14E−5(3.00)

$$u(x, y, 0) = \sin\left(2\pi(x + y)\right) \tag{34}$$

and periodic boundary conditions. The exact solution is

$$u(x, y, t) = \sin\left(2\pi(x + y - 2t)\right).$$

The time step is taken as $\Delta t = 0.25\Delta x$. Table 5 shows the L^1 errors and convergence rates, respectively, at $t = 2.0$. We see that the errors decrease in the sequence of WENO-JS, WENO-Z3, WENO-P3, WENO-R3, and WENO-Rp3. Only the present WENO-Rp3 scheme attains third order. However, the present WENO-R3 scheme also has much smaller errors than the previous third-order WENO schemes.

Example 3 (Long time integration of a jump). We show the performance of the present scheme for long time integration of a jump. We first test numerical schemes on the 1D linear equation (31) with the initial data

$$u_0(x) = \begin{cases} -\sin(\pi x) - \frac{1}{2}x^3, & -1 < x \le 0, \\ -\sin(\pi x) - \frac{1}{2}x^3 + 1, & 0 < x \le 1, \end{cases} \tag{35}$$

which is a piecewise sine function with a jump discontinuity at $x = 0$.

We solve this problem up to $t = 40$ to see behaviors of various schemes at the jump discontinuity. Figure 2 shows comparison of numerical solutions of different WENO schemes using grid points $N = 400$ with the analytical solution. We can see that both the WENO-Rp3 and WENO-R3 schemes match the exact solution very well, and the amount of dissipation is WENO-JS3 > WENO-Z3 > WENO-N3 > WENO-P3 > WENO-R3 ≈ WENO-Rp3.

TABLE 5 L^1 errors and convergence rates at $t = 2.0$ of different schemes for the 2D linear advection Equation (33) with the initial data (34)

	WENO-JS3	WENO-Z3	WENO-N3	WENO-P3	WENO-R3	WENO-Rp3
N	L^1 error (order)	L^1 error (order)	L^1 error (order)	L^1 error (order)	L^1 error (order)	L^1 error (order)
10^2	0.564E−0(—)	0.524E−0(—)	0.505E−0(—)	0.464E−0(—)	0.291E−0(—)	0.260E−0(—)
20^2	0.284E−0(0.99)	0.151E−0(1.80)	0.121E−0(2.06)	8.89E−2(2.38)	4.38E−2(2.73)	4.14E−2(2.65)
40^2	9.15E−2(1.63)	5.74E−2(1.40)	4.32E−2(1.49)	2.80E−2(1.67)	8.21E−3(2.42)	5.36E−3(2.95)
80^2	2.93E−2(1.64)	1.34E−2(2.10)	9.26E−3(2.22)	6.02E−3(2.22)	1.54E−3(2.41)	6.73E−4(2.99)
160^2	5.92E−3(2.31)	2.87E−3(2.22)	1.91E−3(2.28)	1.19E−3(2.34)	3.08E−4(2.32)	8.42E−5(3.00)
320^2	8.31E−4(2.83)	5.99E−4(2.26)	3.74E−4(2.35)	2.31E−4(2.36)	5.50E−5(2.49)	1.05E−5(3.00)
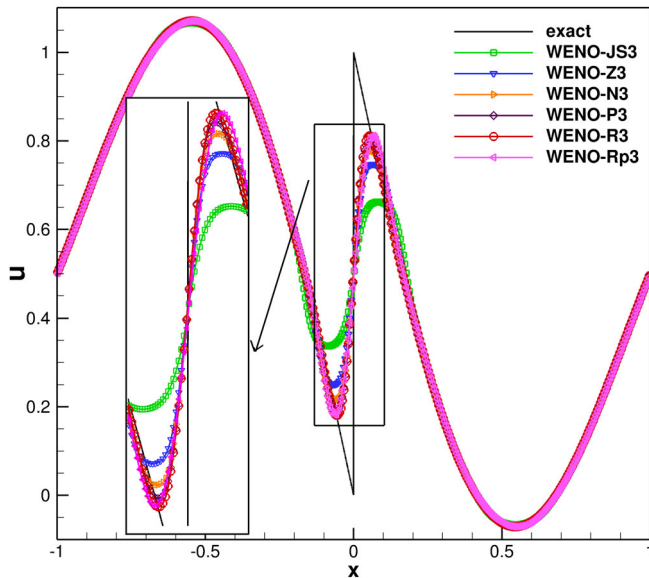
FIGURE 2 Comparison of the analytical and numerical solutions of the linear advection Equation (31) with the initial condition (35) with WENO-JS3, WENO-Z3, WENO-N3, WENO-P3, and the present WENO-R3, and WENO-Rp3 at $t = 40$. Closer-up in the region $x \in [-0.12, 0.12]$ [Colour figure can be viewed at wileyonlinelibrary.com]

We further consider a square wave problem defined by Equation (31) with the initial condition

$$u_0(x) = \begin{cases} 1 & \text{if } -0.5 \leq x \leq 0.5, \\ 0 & \text{otherwise.} \end{cases} \tag{36}$$

We solve this problem up to $t = 40$ in the computational domain $-1 \leq x \leq 1$ with the grid size $\Delta x = 0.01$.

The Courant-Friedrichs-Lewy (CFL) number is set to 0.5. The numerical results are shown in Figure 3. We see that the WENO-Rp3/R3 are less dissipative than WENO-JS3, WENO-Z3, WENO-N3, WENO-P3.

Example 4 (Solution with smooth and discontinuous waves). At last, we solve the 1D linear equation (31) with the following initial condition which contains a Gaussian, a square-wave, a triangle, and a semiellipse wave, given by

$$u_0(x) = \begin{cases} \frac{1}{6}\left(G(x, \beta, z - \delta) + G(x, \beta, z + \delta) + 4G(x, \beta, z)\right), & -0.8 \leq x \leq -0.6, \\ 1, & -0.4 \leq x \leq -0.2, \\ 1 - |10(x - 0.1)|, & 0.0 < x \leq 0.2, \\ \frac{1}{6}\left(F(x, \alpha, a - \delta) + G(x, \alpha, a + \delta) + 4G(x, \alpha, a)\right), & 0.4 \leq x \leq 0.6, \\ 0, & \text{otherwise.} \end{cases} \tag{37}$$

Here, $G(x, \beta, z) = \exp^{-\beta(x-z)^2}$, $F(x, \alpha, a) = \sqrt{\max(1 - \alpha^2(x - a)^2, 0)}$, $a = 0.5, z = -0.7$, $\delta = 0.005$, $\alpha = 10$, and $\beta = \log 2 / 36\delta^2$. The solution of this case consists of contact discontinuities, corner singularities, and smooth areas. We solve this problem with $\Delta t = 0.5\Delta x$ up to $t = 6$. The numerical results are shown in Figure 4. Again, it is seen that the present

FIGURE 3 Comparison of the analytical and numerical solutions of the linear advection with the initial condition (36) with WENO-JS3, WENO-Z3, WENO-N3, WENO-P3, WENO-R3, and WENO-Rp3 at $t = 40$, $N = 200$ [Colour figure can be viewed at wileyonlinelibrary.com]
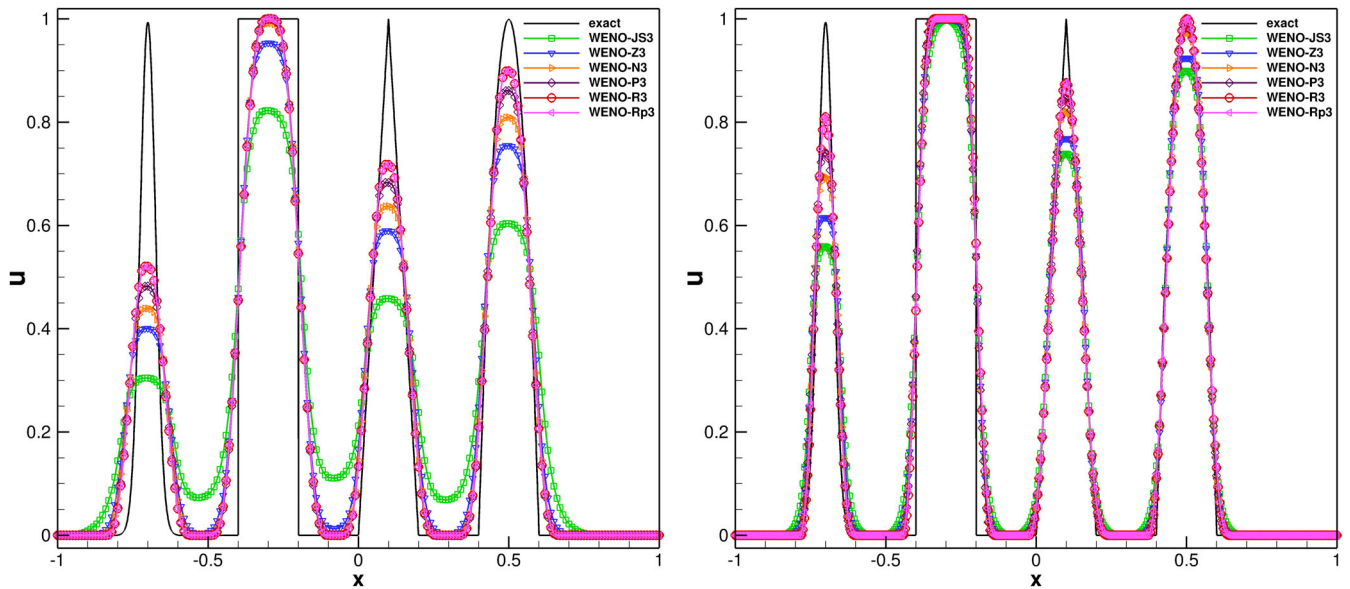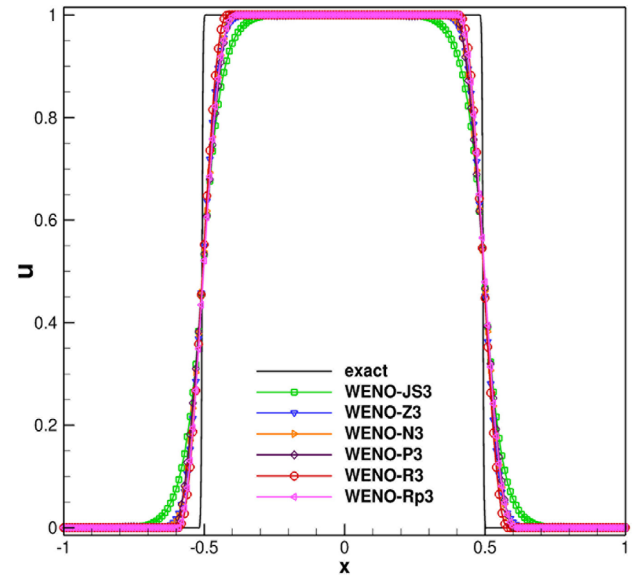
FIGURE 4 Comparison of the analytical and numerical solutions of Equation (31) with the initial condition (37) computed with WENO-JS3, WENO-Z3, WENO-N3, WENO-P3, and WENO-R3 at $t = 6$ with 200 points (left) and 400 grid points (right) [Colour figure can be viewed at wileyonlinelibrary.com]

WENO-Rp3/R3 schemes perform better than WENO-JS3, WENO-Z3, WENO-N3, and WENO-P3, especially near the discontinuities. All the improved third-order WENO schemes produce shaper results than the classical WENO-JS3 scheme, with the present schemes being least dissipative.

4.2 | One-dimensional Euler systems

In this section, we present numerical results for system of hyperbolic conservation laws. We consider the system of 1D Euler equations,

$$U_t + F(U)_x = 0, \tag{38}$$

with

$$U = (\rho, \rho u, E)^T, \quad F(U) = \left(\rho u, \rho u^2 + p, u(E + p)\right)^T.$$

The equation of state is given by

$$p = (\gamma - 1)\left(E - \frac{1}{2}\rho u^2\right),$$

where ρ, u, p, and E are the density, velocity, pressure, and total energy, respectively, and γ is the ratio of specific heats and is taken as 1.4 in all test cases unless otherwise specified. The eigenvalues of the Jacobian matrix $A(U) = \frac{\partial F}{\partial U}$ are

$$\lambda_1 = u - c, \quad \lambda_2 = u, \quad \lambda_3 = u + c,$$

where $c = (\gamma p/\rho)^{1/2}$ is the sound speed. The characteristic decomposition and local Lax-Friedrichs splitting in the characteristic fields[4] are chosen to generalize the WENO schemes to the 1D Euler system.

Example 5 (Accuracy test for the Euler system). First, we consider the periodic solution of the Euler equations (38). The initial values are given by

$$(\rho, u, p) = (1.0 + 0.2\sin(\pi x), 1.0, 1.0), \quad -1 \le x \le 1. \tag{39}$$

Periodic boundary conditions are applied in this test. The exact solution of density is

$$\rho(x, t) = 1.0 + 0.2\sin(\pi(x - t)).$$

The final time is $t = 1.0$. Table 6 shows the L^1 errors and numerical convergence orders of the density at $t = 1.0$ by using different third-order WENO schemes. We can see that the errors decrease in the sequence of WENO-JS3, WENO-Z3, WENO-P3, WENO-R3, and WENO-Rp3. The WENO-R3 scheme has much smaller errors than previous third-order schemes, and the WENO-Rp3 scheme has the smallest errors and achieves the optimal accuracy.

Second, we consider several 1D Riemann problems in which the initial data are of the form

$$U(x, 0) = \begin{cases} U_L & \text{if} \quad x \le x_0, \\ U_R & \text{if} \quad x > x_0. \end{cases}$$

**Example 6** (The Sod problem). Sod's shock tube problem[31,32] has the initial condition given by

$$(\rho, u, p) = \begin{cases} (1.000, 0.000, 1.000), & \text{if} \quad 0 \le x < 0.5, \\ (0.125, 0.000, 0.100), & \text{if} \quad 0.5 \le x \le 1, \end{cases}$$

We solve the problem up to $t = 0.2$ with $\Delta x = 0.005$. The numerical results of the density field with different schemes are compared with the exact Riemann solution[33] in Figure 5. It can be seen that the results of the WENO-P3 and WENO-R3

TABLE 6 L^1 errors and convergence rates of the density at $t = 1.0$ of different schemes for the 1D Euler equations (38) with the initial data (39)

	WENO-JS3	WENO-Z3	WENO-N3	WENO-P3	WENO-R3	WENO-Rp3
N	L^1 error (order)	L^1 error (order)	L^1 error (order)	L^1 error (order)	L^1 error (order)	L^1 error (order)
10	3.14E−2(—)	2.25E−2(—)	1.99E−2(—)	1.69E−2(—)	1.36E−2(—)	8.56E−3(—)
20	1.36E−2(1.21)	9.67E−3(1.22)	8.33E−3(1.26)	6.24E−3(1.44)	3.95E−3(1.78)	1.07E−3(3.00)
40	4.36E−3(1.64)	2.51E−3(1.95)	2.03E−3(2.04)	1.46E−3(2.10)	9.49E−4(2.06)	1.40E−4(2.94)
80	1.11E−3(1.97)	5.86E−4(2.10)	4.76E−4(2.09)	3.28E−4(2.15)	2.07E−4(2.20)	1.77E−5(2.98)
160	2.73E−4(2.02)	1.32E−4(2.15)	1.01E−4(2.19)	7.01E−5(2.22)	4.43E−5(2.22)	2.62E−6(2.76)
320	6.50E−5(2.07)	2.90E−5(2.19)	2.19E−5(2.21)	1.46E−5(2.26)	9.34E−6(2.25)	3.27E−7(3.00)

FIGURE 5 Numerical results of Sod problem[32] with MUSCL-Van Leer, WENO-JS3, WENO-Z3, WENO-P3, and WENO-R3 at $t = 0.2$, $N = 200$, CFL = 0.6. The subset is the zoom of the contact wave of density. [Colour figure can be viewed at wileyonlinelibrary.com]
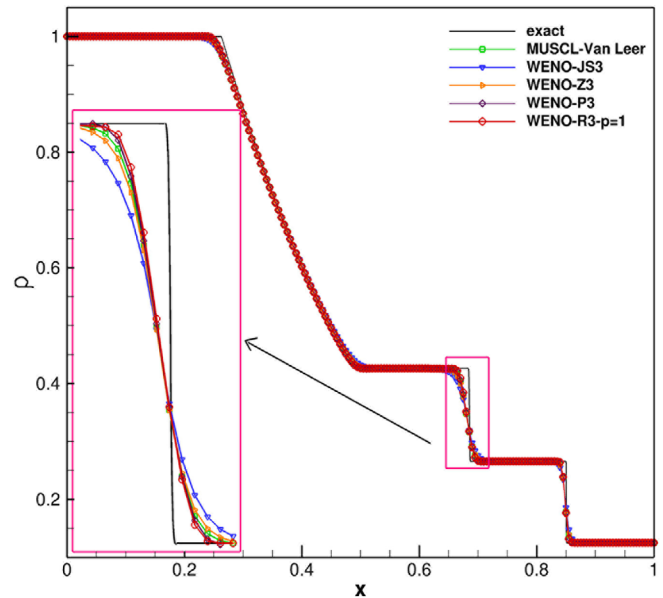

schemes are shaper than the MUSCL result, while the result of the WENO-JS3 is less shaper than the MUSCL result, and that of the WENO-Z3 is comparable to the MUSCL result. The WENO-R3 scheme is in best agreement with the exact solution. Figure 6 shows comparison between the WENO-Rp3 and WENO-R3 schemes. We see that the WENO-Rp3 produces unacceptable overshoot and undershoot at the discontinuities and rarefaction waves, so this scheme is not recommended.

Example 7 (The Lax problem). The Lax problem[31,32] has the initial condition given by

$$(\rho, u, p) = \begin{cases} (0.445, 0.698, 0.3528), & \text{if} \quad 0 \leq x < 0.5, \\ (0.500, 0.000, 0.5710), & \text{if} \quad 0.5 \leq x \leq 1. \end{cases}$$

We solve the problem up to $t = 0.13$ with $\Delta x = 0.05$. The numerical results of the density field are displayed in Figure 7. It is seen that the WENO-R3 performs better than the WENO-P3, WENO-Z3, MUSCL-Van Leer, and WENO-JS3 schemes. The third-order WENO-JS3 scheme is even more dissipative than the third-order MUSCL3-LF scheme. Figure 8 compares the WENO-Rp3 ($p = 1.5$) and WENO-R3 ($p = 1$) schemes. Again we see that the WENO-Rp3 scheme generates evident
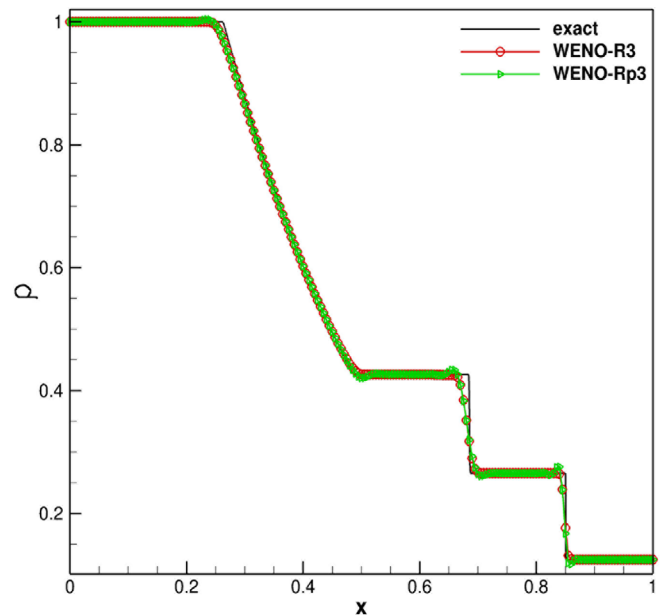
FIGURE 6 Comparison between the WENO-R3 and WENO-Rp3 schemes for Sod problem[32] at $t = 0.2$, $N = 200$, CFL = 0.6 [Colour figure can be viewed at wileyonlinelibrary.com]
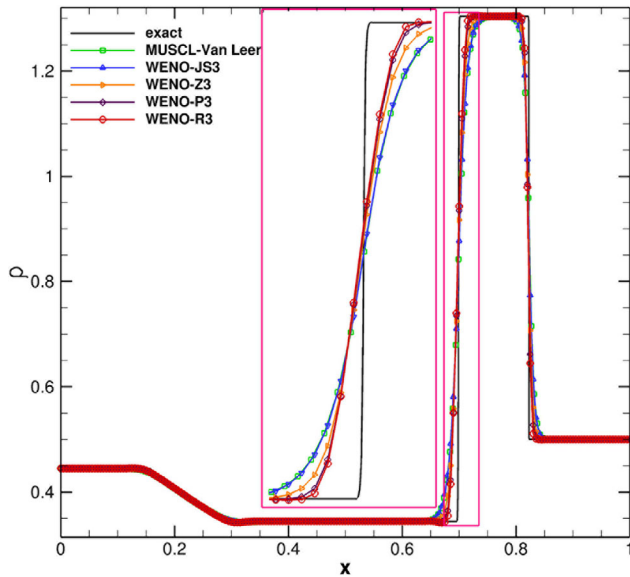
FIGURE 7 Numerical results of Lax problem[32] with MUSCL3-Van Leer, WENO-JS3, WENO-Z3, WENO-P3, and WENO-R3 at $t = 0.13$, $N = 200$, CFL = 0.6. The subset shows the zoom of the contact wave [Colour figure can be viewed at wileyonlinelibrary.com]
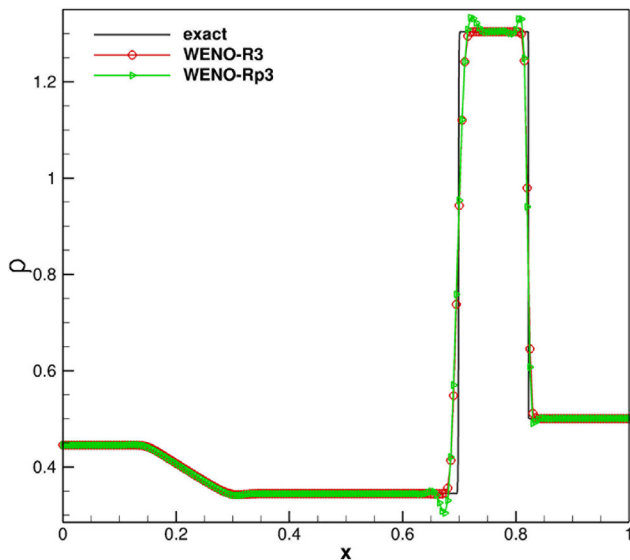
FIGURE 8 Numerical results of Lax problem[32] with WENO-R3 and WENO-Rp3 at $t = 0.13$, $N = 200$, CFL = 0.6 [Colour figure can be viewed at wileyonlinelibrary.com]

oscillations at the contact discontinuity and shock. So the WENO-Rp3 scheme is not recommended and will not be used in the following examples.

Example 8 (Shock-entropy wave interaction[5]). We compute the approximate solution on the domain $[-5, 5]$ with periodic boundary conditions. The initial condition is given by

$$(\rho, u, p) = \begin{cases} \left(\frac{27}{7}, \frac{4\sqrt{35}}{9}, \frac{31}{3} \right), & \text{if } -5 \leq x < -4, \\ (1 + \epsilon \sin(kx), 0, 1), & \text{if } -4 \leq x \leq 5, \end{cases}$$

where ϵ and k are the amplitude and wave number of the entropy wave, respectively. Here, we set $\epsilon = 0.2$ and $k = 5$. In this problem, a right-moving supersonic (Mach 3) shock wave interacts with sine waves in a density disturbance that generates a flow field with both smooth structures and discontinuities. The flow induces wave trails behind the right-going shock at wave numbers higher than the initial density-variation wave number k. Since the exact solution is unknown, the reference solution is obtained by using the fifth-order WENO-JS scheme[6] with 3201 grid points. Figure 9 compares comparison of the numerical results for density profiles with the reference solution. It can be seen that the WENO-R3 scheme captures the high-frequency waves behind the right-going shock better than the WENO-P3, WENO-Z3, MUSCL3, and WENO-JS3 schemes.

FIGURE 9 Density profiles of the shock-entropy wave interaction[5] computed with MUSCL3-Van Leer, WENO-JS3, WENO-Z3, WENO-P3, and WENO-R3 at $t = 1.8$ with 401 points and CFL = 0.5 [Colour figure can be viewed at wileyonlinelibrary.com]
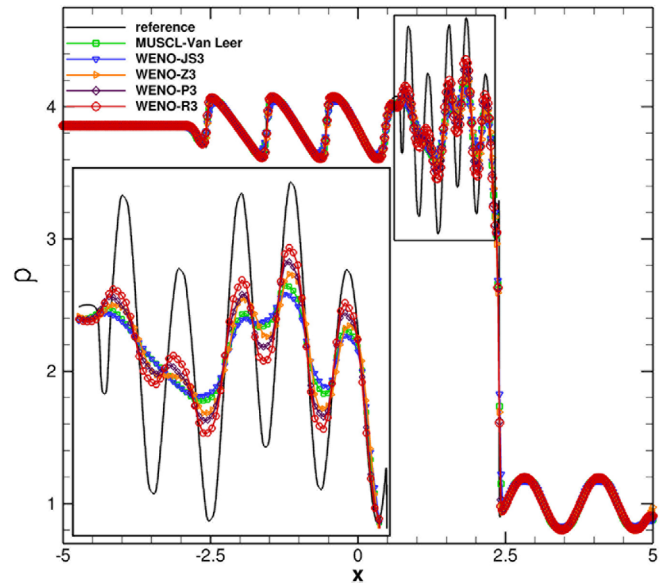
Example 9 (Shock-entropy wave test of Titarev-Toro[34]). This is a variation of the Shu-Osher problem[5] with a different initial condition given as follows

$$(\rho, u, p) = \begin{cases} (1.515695, 0.523346, 1.805000), & \text{if } -5 \leq x < -4.5, \\ (1 + 0.1 \sin(20\pi x), 0, 1), & \text{if } -4.5 \leq x \leq 5. \end{cases}$$

The flow contains physical oscillations which have to be resolved by the numerical method. We compute the solution until the output time $t = 5$. Figure 10 depicts comparison of results for all schemes on a mesh of 4000 cells. The reference solution is obtained by applying the WENO-R3 scheme on a fine mesh of 6400 cells. It is obvious that the present WENO-R3 scheme resolves most of the waves with a good approximation of the wave amplitudes better than other tested schemes. Unlike in Example 8, the MUSCL3 scheme for this case shows a higher resolution compared with the WENO-Z3 scheme.

Example 10 (Interacting blast waves[31,32]). This problem has the initial condition given as

$$(\rho, u, p) = \begin{cases} (1, 0, 1000), & \text{if } 0 \leq x < 0.1, \\ (1, 0, 0.01), & \text{if } 0.1 \leq x < 0.9, \\ (1, 0, 100), & \text{if } 0.9 \leq x \leq 1, \end{cases}$$

with reflective boundary conditions at both ends since the waves generated by the initial discontinuity have arrived at both ends at the output time $t = 0.038$. We solve this problem up to $t = 0.038$ with $\Delta x = 0.0025$. The numerical results of the density distribution are displayed in Figure 11. The WENO-R3 and WENO-P3 schemes produce overshoots at $x \approx 0.57$ and $x \approx 0.8$. From the enlarged frame, we again see that the amount of dissipation near discontinuities is WENO-R3 < WENO-P3 < WENO-Z3 < MUSCL3 < WENO-JS3.

4.3 | Two-dimensional Euler systems

In this subsection we apply the present WENO-R3 scheme to the 2D compressible Euler systems of the form,

$$U_t + F(U)_x + G(U)_y = 0, \tag{40}$$
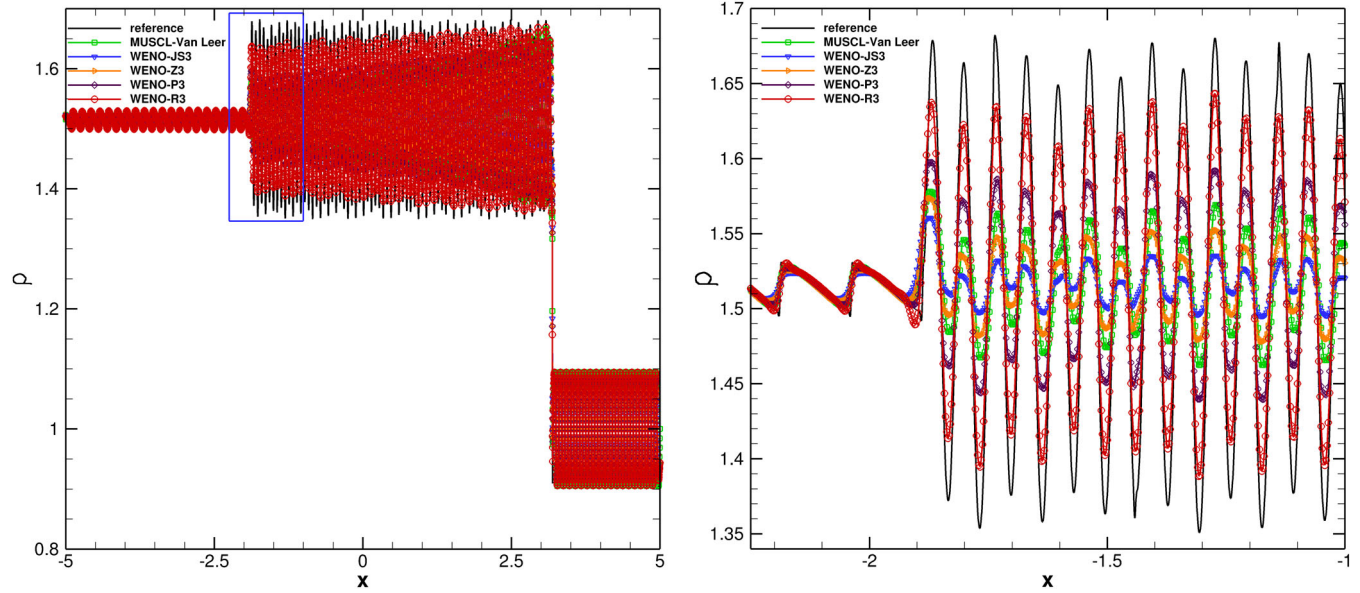
FIGURE 10 Density profiles of shock-entropy wave test of Titarev-Toro[34] computed with different third-order schemes at $t = 5$ with 4001 points and CFL = 0.5. The right frame shows the partial view [Colour figure can be viewed at wileyonlinelibrary.com]
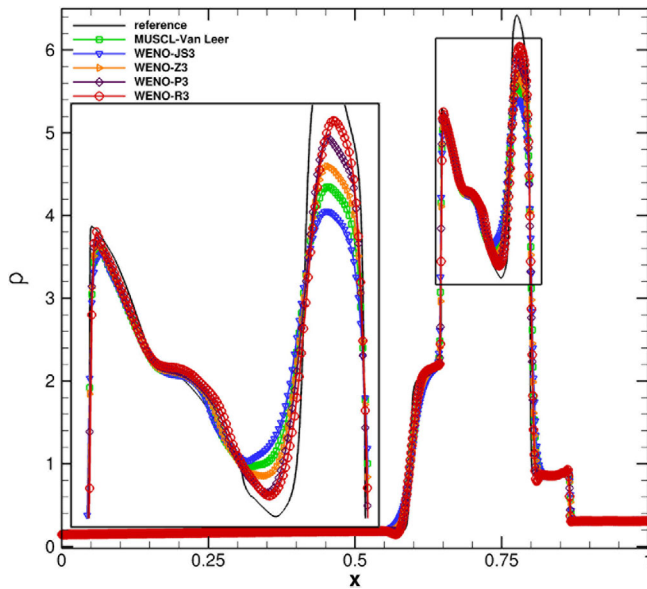
FIGURE 11 Numerical results of interacting blast waves[32] with MUSCL3-Van Leer, WENO-JS3, WENO-Z3, WENO-P3, and WENO-R3 at $t = 0.038$, $N = 400$, CFL = 0.6. Density profile and zoom of the contact wave of density. The reference solution is obtained by applying the WENO-Z3 scheme on a fine mesh of 6400 cells [Colour figure can be viewed at wileyonlinelibrary.com]

where

$$U = (\rho, \rho u, \rho v, E)^T,$$
$$F(U) = (\rho u, \rho u^2 + p, \rho uv, u(E + p))^T,$$
$$G(U) = (\rho v, \rho vu, \rho v^2 + p, v(E + p))^T,$$
$$p = (\gamma - 1)\left(E - \frac{1}{2}\rho(u^2 + v^2)\right).$$

Here $\rho, u, v, p,$ and E are density, components of velocity in the x and y coordinate directions, pressure, and total energy, respectively. $\gamma = 1.4$ is used for all cases. Also, U is the vector of conservative variables, $F(U)$ the x-wise-flux component, and $G(U)$ the y-wise-flux component. The 2D Euler system (40) are solved in a dimension-by-dimension fashion and for each direction the reconstructions in the characteristic fields are used.

Example 11 (Two-dimensional Riemann Problem for gas dynamics[35]). The computational domain is the square $[0, 1] \times [0, 1]$. The 2D Riemann problem is defined by four constant states on each of four quadrants which is divided by lines $x = 0.8$ and $y = 0.8$ on the square:

$$(\rho, u, v, p) = \begin{cases} (1.5, 0, 0, 1.5), & 0.8 \leq x \leq 1, \ 0.8 \leq y \leq 1, \\ (0.5323, 1.206, 0, 0.3), & 0 \leq x < 0.8, \ 0.8 \leq y \leq 1, \\ (0.138, 1.206, 1.206, 0.029), & 0 \leq x \leq 0.8, \ 0 \leq y < 0.8, \\ (0.5323, 0, 1.206, 0.3), & 0.8 < x \leq 1, \ 0 \leq y < 0.8, \end{cases}$$

and transmissive boundary conditions.

We solve this problem until time $t = 0.8$ with CFL $= 0.6$. Figure 12 shows the numerical results obtained with different third-order WENO schemes and the MUSCL-Van Leer scheme. An examination of these results reveals that the WENO-R3
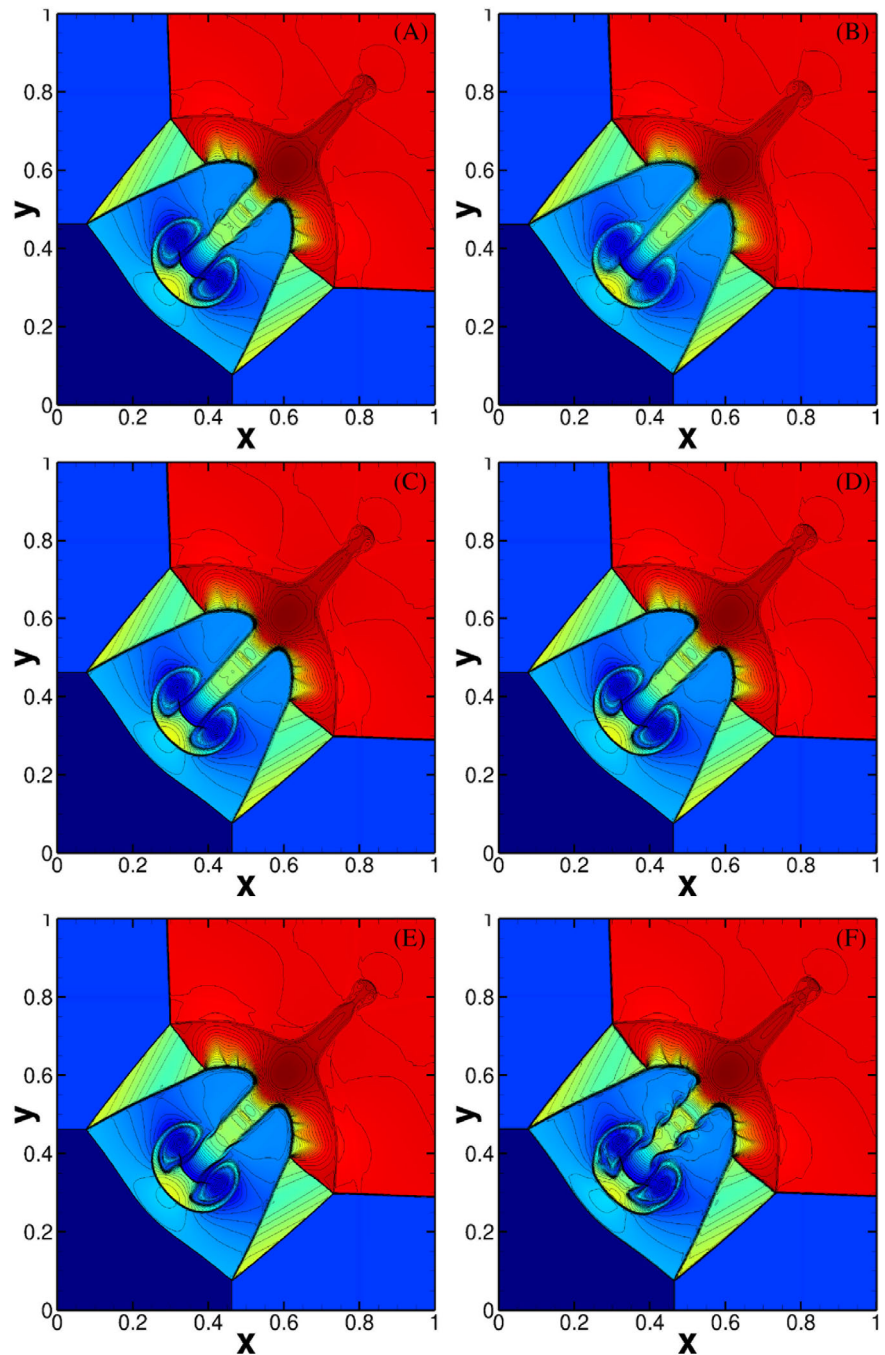

FIGURE 12 Density contours of 2D Riemann Problem[35] with 50 contour lines ranging from 0.2 to 1.7 on 801×801 grid points at $t = 0.8$. (A) MUSCL3-Van Leer, (B) WENO-JS3, (C) WENO-Z3, (D) WENO-N3, (E) WENO-P3, (F) WENO-R3 [Colour figure can be viewed at wileyonlinelibrary.com]

scheme has the best resolution of the structure on the slip lines. The WENO-P3 and WENO-N3 schemes have similar resolution. The MUSCL3-Van Leer scheme is more dissipative than the WENO-N3 but is comparable to the WENO-Z3 scheme, and the WENO-JS3 scheme is most dissipative.

Example 12 (Double Mach reflection of a strong shock[36]). The two-dimensional double Mach reflection problem describes the reflection of a planar shock in air hitting a wedge. This test is widely used to verify the performance of numerical methods. We calculate this test problem on $[0, 4] \times [0, 1]$ and display the results in $[0, 3] \times [0, 1]$ as usual. Initially a right moving Mach 10 shock is imposed and the shock front makes an angle of 60° with the x-axis at $x = 1/6$. The region from $x = 0$ to $x = 1/6$ along the bottom boundary is assigned values of the initial postshock flow and reflecting boundary condition is taken for the rest. The left boundary is assigned values of the initial postshock flow. For the right-hand boundary at $x = 4$, all gradients are set to zero. The top boundary of the problem is set to describe the exact motion of the Mach 10 shock. See Reference 36 for a detailed description. We compute the problem to $t = 0.2$ with $\Delta x = \Delta y = 1/480$ and CFL $= 0.6$. The numerical results of the WENO-R3 scheme are compared with those of the MUSCL3, WENO-JS3, WENO-Z3, WENO-N3, and WENO-P3 schemes in Figure 13. It can be clearly seen that the WENO-R3 scheme resolves better the
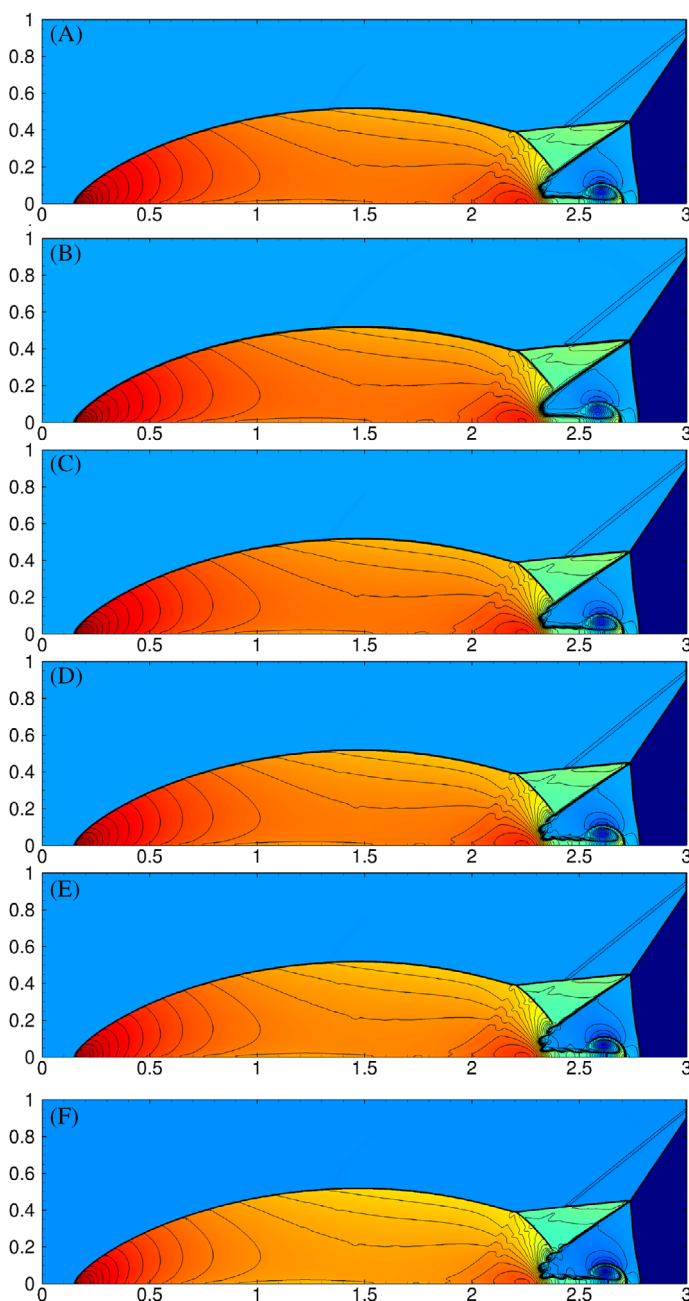

FIGURE 13 Density contours of Double Mach reflection problem at $t = 0.2$ with 1920×480 grid points. From top to bottom: (A) MUSCL3-Van Leer, (B) WENO-JS3, (C) WENO-Z3, (D) WENO-N3, (E) WENO-P3, (F) WENO-R3 [Colour figure can be viewed at wileyonlinelibrary.com]
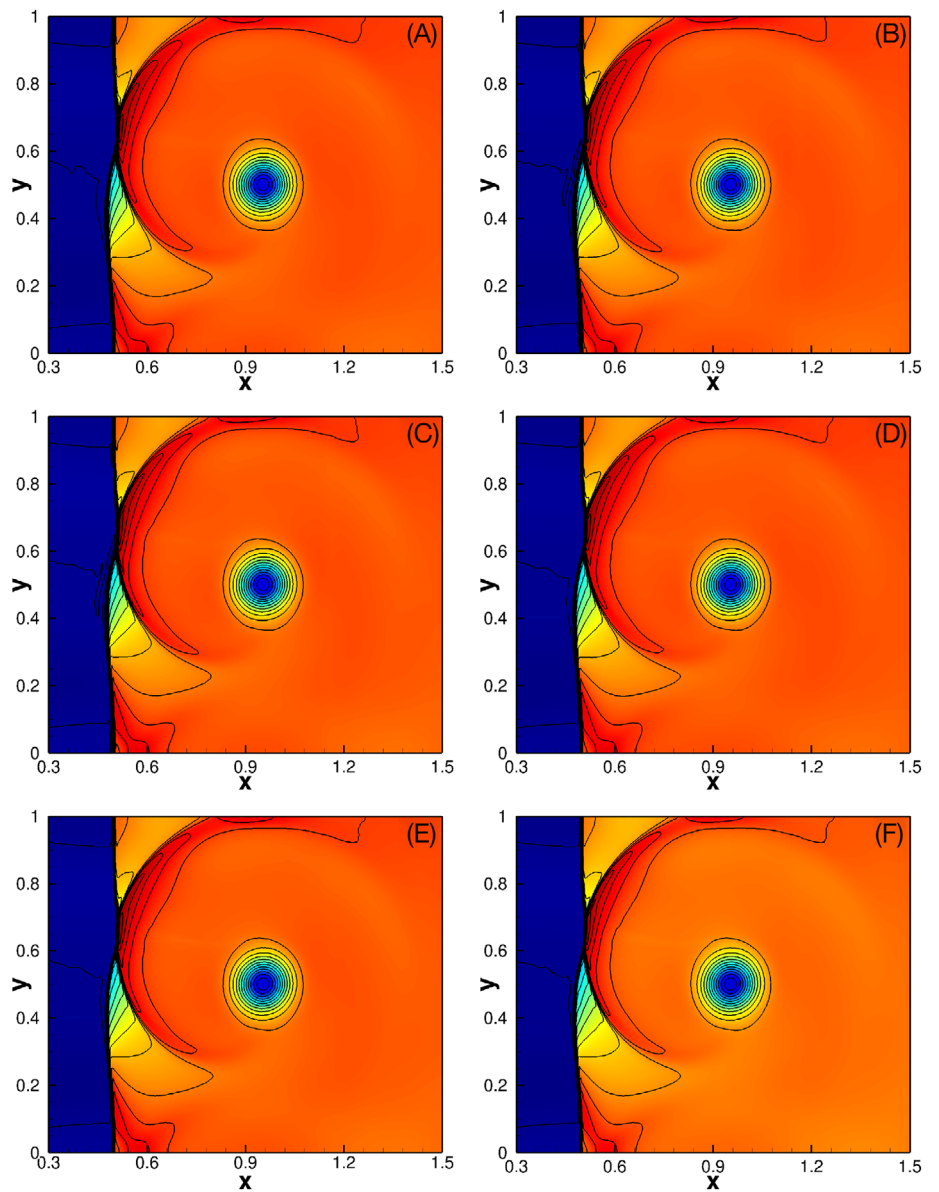
FIGURE 14 Density contours of 2D inviscid shock/vortex interactions computed with (A) MUSCL3-Van Leer, (B) WENO-JS3, (C) WENO-Z, (D) WENO-N3, (E) WENO-P3, (F) WENO-R3 schemes at $t = 0.6$ on 500×200 grid cells [Colour figure can be viewed at wileyonlinelibrary.com]
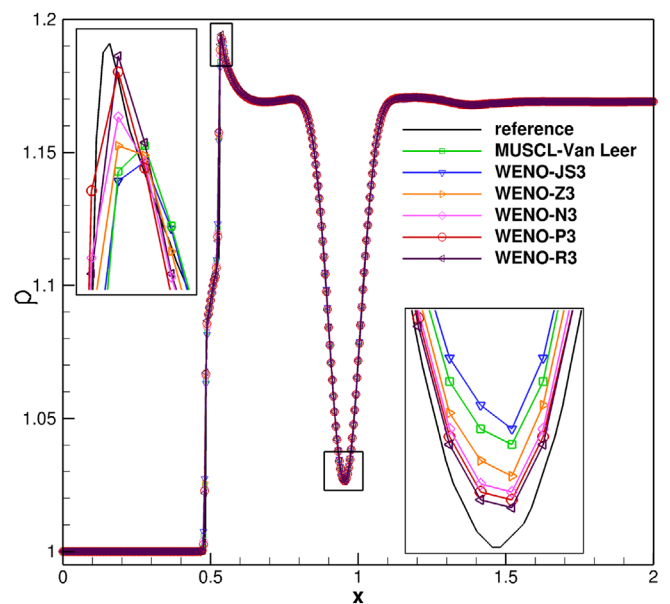
FIGURE 15 Instantaneous density distribution of the shock-vortex interaction problem at $t = 0.6$ along the line $y = 0.5$ computed by different schemes on a grid of 500×200. The reference is computed by WENO-Z3 on the 2000×800 grid [Colour figure can be viewed at wileyonlinelibrary.com]
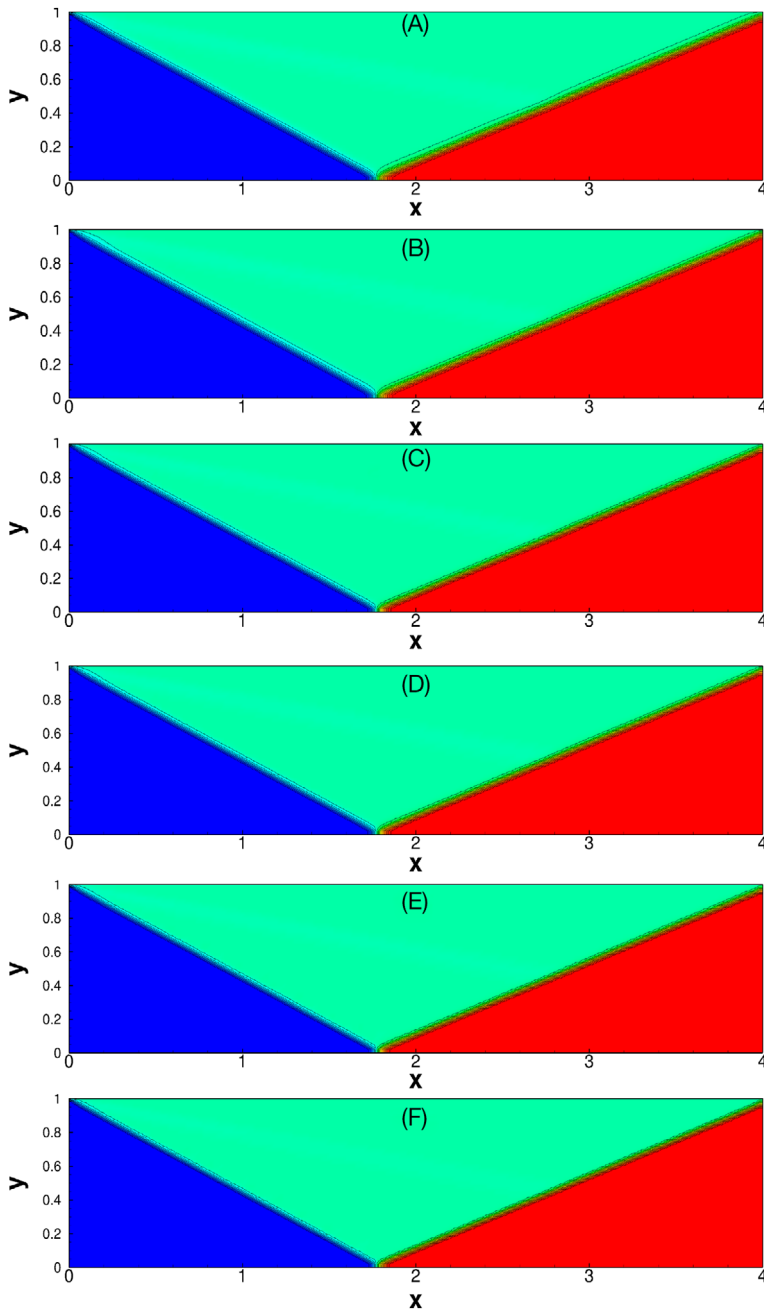
FIGURE 16 Density contours of the 2D shock regular reflection problem computed with (A) MUSCL3-Van Leer,(B) WENO-JS3, (C) WENO-Z, (D) WENO-N3, (E) WENO-P3, (F) WENO-R3 schemes at $t = 20$ with 200×50 grid cells [Colour figure can be viewed at wileyonlinelibrary.com]

instabilities around the Mach stem. The resolution from (a) to (f) is gradually increased except that the MUSCL3 (a) has a comparable resolution with the WENO-Z3 (c).

Example 13 (Two-dimensional inviscid shock/vortex interactions[29]). This two-dimensional example contains an interaction between a stationary Mach 1.1 shock and a moving isentropic vortex. The initial condition is set as the exact Rankine-Hugoniot condition and a vortex is added to the main flow with its center at $(x_0, y_0) = (0.25, 0.5)$. The left and right states of the shock are specified as

$$(\rho, u, v, p) = \begin{cases} (1, 1.1\sqrt{\gamma}, 0, 1), & \text{if } 0.0 \le x < 0.5, \\ (1.169, 1.1134, 0, 1.245), & \text{if } 0.5 \le x \le 2. \end{cases}$$

The vortex is described by the perturbations to the velocities (u, v), temperature $(T = p/\rho)$, and entropy $(S = \ln(p/\rho^{\gamma}))$ of the mean flow which have the values

$$u' = \epsilon\tau\exp^{\alpha(1-\tau^2)}\sin\theta, \tag{41a}$$

$$v' = -\epsilon\tau\exp^{\alpha(1-\tau^2)}\cos\theta, \tag{41b}$$

$$T' = \frac{(\gamma-1)\epsilon^2\exp^{2\alpha(1-\tau^2)}}{4\alpha\gamma}, \tag{41c}$$

$$S' = 0, \tag{41d}$$

where $\tau = r/r_c$, $r = \sqrt{(x-x_0)^2 + (y-y_0)^2}$, $\epsilon = 0.3, r_c = 0.05$, and $\alpha = 0.204$. A nondimensional computational domain $[0, 2] \times [0, 1]$ is used. Transmissive boundary conditions are imposed on the boundary and the final time is taken as $t = 0.5$. We solve this problem to the time $t = 0.6$ using 500×200 cells with CFL $= 0.6$. Figure 14 shows the details of the computed density contours, and Figure 15 compares the density profiles on the line of $y = 0.5$, which clearly indicates that the WENO-R3 scheme has a higher resolution compared with other schemes.

Example 14 (Two-dimensional regular shock reflection[37]). The purpose of this example is to verify if the new scheme can obtain steady state solution. A shock impinges the bottom wall with an angle of $\theta = 29°$ and is regularly reflected from the wall. The inflow Mach number is 2.9. The computational domain is $[0, 4] \times [0, 1]$ which is divided into 200×50 equally spaced grids. The boundary conditions on the left and top boundaries of the domain are supersonic inflow

$$(\rho, u, v, p)_1 = (1.4, 2.9, 0, 1),$$
$$(\rho, u, v, p)_2 = (2.38, 2.6193, -0.50632, 2.13948).$$

The bottom boundary is a reflecting wall and the right one is supersonic outflow. Figure 16 shows the computed density contours at $t = 50$ when the solution has reached steady state. Figure 17A shows the density distributions along the line $y = 0.5$. We see that the results of the present WENO-R3 scheme is most close to the exact solution. Figure 17B shows the evolution of the maximal density residual with time. It can be clearly seen that the WENO-R3 scheme can converge to about 10^{-12} as other third-order schemes.
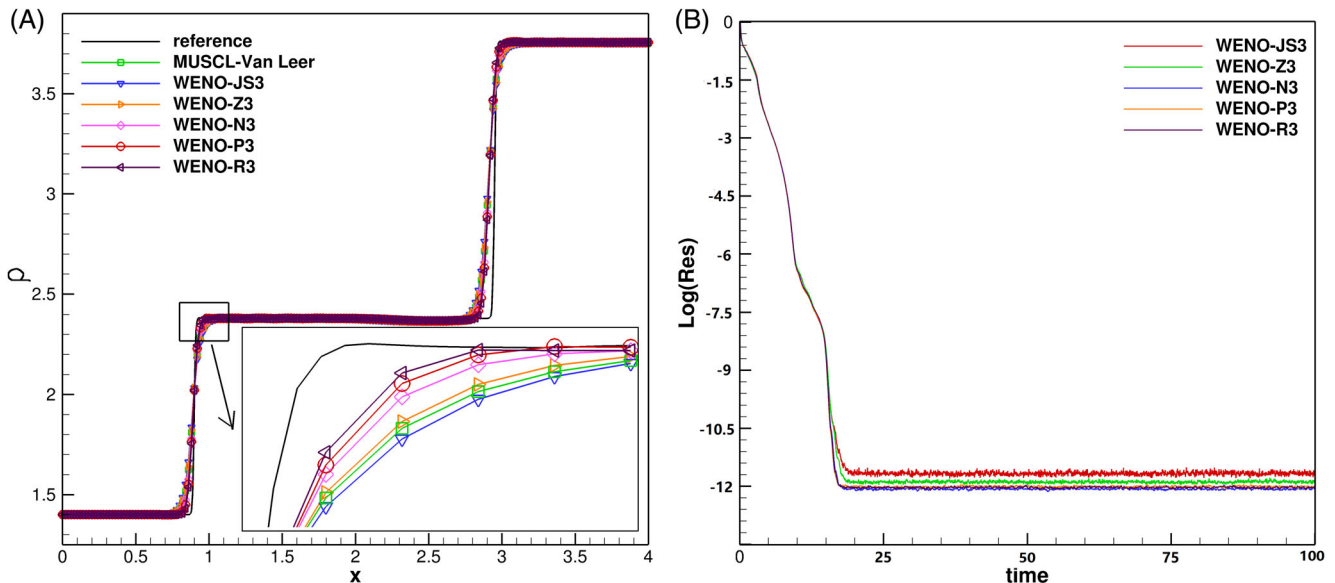
FIGURE 17 The regular shock reflection problem computed with different schemes. (A) Density distribution at $t = 50$ along $y = 0.5$ by a grid 200×50. (B) Time history of the max density residual (density residual is in terms of $\Delta\rho/\Delta t$) [Colour figure can be viewed at wileyonlinelibrary.com]

5 | CONCLUSION

We develop a low-dissipation third-order WENO scheme (WENO-R3) for the numerical solution of nonlinear hyperbolic conservation laws by introducing a new reference smoothness indicator in the WENO-Z weights. The new reference smoothness indicator is a nonlinear combination of the Jiang-Shu smoothness indicators for local and global stencils. The proposed scheme achieves third-order accuracy in smooth regions without critical points. A number of one- and two-dimensional linear scalar convection equation and Euler equation problems are calculated. The numerical results show that the WENO-R3 scheme resolves discontinuities and small-scale structures better than several recently developed third-order WENO schemes and the popular third-order MUSCL scheme.

ORCID
Li Yuan https://orcid.org/0000-0003-1397-9089

REFERENCES
1. Liu XD, Osher S, Chan T. Weighted essentially non-oscillatory schemes. *J Comput Phys.* 1994;115:200-212.
2. Harten A, Osher S. Uniformly high-order accurate non-oscillatory schemes I. *SIAM J Numer Anal.* 1987;24(2):279-309.
3. Harten A, Engquist B, Osher S, Chakravarthy S. Uniformly high-order accurate non-oscillatory schemes III. *J Comput Phys.* 1987;71:231-303.
4. Shu CW, Osher S. Efficient implementation of essentially non-oscillatory shock capturing schemes. *J Comput Phys.* 1988;77:439-471.
5. Shu CW, Osher S. Efficient implementation of essentially non-oscillatory shock capturing schemes II. *J Comput Phys.* 1989;83:32-78.
6. Jiang GS, Shu CW. Efficient implementation of weighted ENO schemes. *J Comput Phys.* 1996;126:202-228.
7. Henrick AK, Aslam TD, Powers JM. Mapped weighted essentially non-oscillatory schemes: Achieving optimal order near critical points. *J Comput Phys.* 2005;207:542-567.
8. Gerolymos GA, Sénéchal D, Vallet I. Very-high-order WENO schemes. *J Comput Phys.* 2009;228:8481-8524.
9. Borges R, Carmona M, Costa B, Don WS. An improved WENO scheme for hyperbolic conservation laws. *J Comput Phys.* 2008;227:3191-3211.
10. Kumar R, Chandrashekar P. Simple smoothness indicator and multi-level adaptive order WENO scheme for hyperbolic conservation laws. *J Comput Phys.* 2018;375:1059-1090.
11. Rathan S, Raju GN. Improved weighted ENO scheme based on parameters involved in nonlinear weights. *Appl Math Comput.* 2018;331:120-129.
12. Kim CH, Ha Y, Yoon J. Modified non-linear weights for fifth-order weighted essentially non-oscillatory schemes. *J Sci Comput.* 2016;67:299-323.
13. Rathan S, Raju GN. A modified fifth-order WENO scheme for hyperbolic conservation laws. *Comput Math App.* 2018;75:1531-1549.
14. Castro M, Costa B, Don WS. High order weighted essentially non-oscillatory WENO-Z schemes for hyperbolic conservation laws. *J Comput Phys.* 2011;230:1766-1792.
15. Rathan S, Raju GN. An improved non-linear weights for seventh-order weighted essentially non-oscillatory scheme. *Comput Fluids.* 2017;156:496-514.
16. Kumar R, Chandrashekar P. Efficient seventh order WENO schemes of adaptive order for hyperbolic conservation laws. *Comput Fluids.* 2019;190:49-76.
17. Don WS, Borges R. Accuracy of the weighted essentially non-oscillatory conservative finite difference schemes. *J Comput Phys.* 2013;250:347-372.
18. Wu X, Zhao Y. A high-resolution hybrid scheme for hyperbolic conservation laws. *Int J Numer Methods Fluids.* 2015;78:162-187.
19. Wu X, Liang J, Zhao Y. A new smoothness indicator for third-order WENO scheme. *Int J Numer Methods Fluids.* 2016;81:451-459.
20. Gande NR, Rathod Y, Rathan S. Third-order WENO scheme with a new smoothness indicator. *Int J Numer Methods Fluids.* 2017;85:90-112.
21. Gande NR, Rathod Y, Samala R. Improved third-order weighted essentially nonoscillatory scheme. *Int J Numer Methods Fluids.* 2018;87:329-342.
22. Zeng FJ, Shen YQ, Liu SP. A perturbational weighted essentially non-oscillatory scheme. *Comput Fluids.* 2018;172:196-208.
23. Xu WZ, Wu WG. An improved third-order WENO-Z Scheme. *J Sci Comput.* 2018;75:1808-1841.
24. Xu WZ, Wu WG. An improved third-order weighted essentially non-oscillatory scheme achieving optimal order near critical points. *Comput Fluids.* 2018;30:113-125.
25. Bhise AA, Gande NR, Rathan S, Devakar M. An efficient hybrid WENO scheme with a problem independent discontinuity locator. *Int J Numer Methods Fluids.* 2019;91:1-28.

26. Liu SP, Shen YQ. Discontinuity-detecting method for a four-point stencil and its application to develop a third-order hybrid-WENO scheme. *J Sci Comput*. 2019;81:1732-1766.

27. van Leer B. Towards the ultimate conservative difference scheme V. A second order sequel to Godunov's method. *J Comput Phys*. 1979;32:101-136.

28. Collela P. A direct Eulerian MUSCL scheme for gas dynamics. *SIAM J Sci Comput*. 1985;6(1):104-117.

29. Shu CW. *Essentially Non-Oscillatory and Weighted Essentially Non-Oscillatory Schemes for Hyperbolic Conservation Laws ICASE Report No. 97-65*. Hampton, VA: NASA Langley Research Center; 1997.

30. Hu XY, Wang Q, Adams NA. An adaptive central-upwind weighted essentially non-oscillatory scheme. *J Comput Phys*. 2010;229:8952-8965.

31. Lax PD. Weak solutions of nonlinear hyperbolic equations and their numerical computation. *Commun Pure Appl Math*. 1954;7:159-193.

32. Sod G. A survey of several finite difference methods for systems of nonlinear hyperbolic conservation laws. *J Comput Phys*. 1978;27:1-31.

33. Toro EF. *Riemann Solvers and Numerical Methods for Fluid Dynamics*. New York, NY: Springer-Verlag; 1997.

34. Titarev VA, Toro EF. Finite-volume WENO schemes for three-dimensional conservation laws. *J Comput Phys*. 2004;201:238-260.

35. Schulz-Rinne CW, Collins JP, Glaz HM. Numerical solution of the Riemann problem for two-dimensional gas dynamics. *SIAM J Sci Comput*. 1993;14(6):1394-1414.

36. Woodward P, Colella P. The numerical simulation of two-dimensional fluid flow with strong shocks. *J Comput Phys*. 1984;54:115-173.

37. Zhang SH, Shu CW. A new smoothness indicator for the WENO schemes and its effect on the convergence to steady state solutions. *J Sci Comput*. 2007;31:273-305.

SUPPORTING INFORMATION

Additional supporting information may be found online in the Supporting Information section at the end of this article.